# Inducing lasing in organic materials with low optical gain by three-dimensional plasmonic nanocavity arrays

Han, Chunrui; Qi, Yuejing; Wang, Yu; Ye, Wanting

*Published in:*
Optics Express

*DOI:*
10.1364/OE.27.020597

Research Article | Vol. 27, No. 15 / 22 July 2019 / Optics Express 20597
Optics EXPRESS

# Inducing lasing in organic materials with low optical gain by three-dimensional plasmonic nanocavity arrays

CHUNRUI HAN,[1,2,3] YUEJING QI,[1] YU WANG,[1] AND JIANTING YE[2,4]

[1] *Institute of Microelectronics, The Chinese Academy of Sciences, Beijing, 100029, China*
[2] *Device Physics of Complex Materials, Zernike Institute for Advanced Materials, University of Groningen, Nijenborgh 4, 9747 AG, Groningen, The Netherlands*
[3] *hanchunrui@ime.ac.cn*
[4] *j.ye@rug.nl*

**Abstract:** Lasing in organic media with very low gain has been pursued for a long time in optoelectronics. Here, we experimentally demonstrate that plasmonic lasing in the visible regime at room temperature can be achieved by hybridizing active media of very low optical gain such as ionic liquid and polymethylmethacrylate with three-dimensional (3D) plasmonic metamaterials. The 3D nanostructure consists of a double-layer N-shaped silver wire-hole array with strongly coupled multiple hot spots densely packed in each unit cell. These hot spots overlap perfectly with the gain media, allowing efficient gain-plasmon coupling in subwavelength volumes. The periodic arrangement of hot spots, as the metal and dielectric are distributed in an alternate manner along both transverse and vertical directions, results in ultrastrong suppression of scattering losses. In addition, the lasing characteristics, including threshold, intensity and polarization can be controlled by the lattice constant and geometry of metamaterials. Such a plasmonic nanolaser proves to be of low threshold and low gain requirement, providing an essential step towards easy-processing organic based optoelectronics.



## 1. Introduction

Compact coherent light sources are the key ingredient for integrated optoelectronic and photonic circuits, offering advanced applications in short-distance optical communication, fast digital signal processing, ultrasensitive bio-chemical sensing and in situ cellular imaging [1–4]. In the past few decades, tremendous efforts have been devoted towards developing small laser cavities using various materials and feedback mechanisms, including Fabry-Pérot (FP) cavity in nanowire lasers [5], whispering-gallery mode cavity in microdisk lasers [6], Bragg grating cavity in photonic crystal lasers [7], and metallic cavities for both non-plasmon [8] and plasmon lasers [9]. Among them, only the metal based plasmon lasers, the so-called SPASERs (surface plasmon amplification by stimulated emission of radiation), are able to go beyond the diffraction limit and enable ultrafast operation up to femtosecond timescales [10,11]. Two types of plasmon modes have been used for plasmon lasers: propagating surface plasmon polaritons (SPP) and localized surface plasmons (LSP). The typical SPP based nanolasers are implemented in a metal-insulator-semiconductor (MIS) configuration and have a hybrid SPP-waveguide mode for the cavity feedback [12–14]. In contrast, LSP lasing relies on the subwavelength confinement of electromagnetic (EM) fields around individual nanoparticles which are arranged in either a large ensemble or a periodic array [15,16].

Despite of the significant progress in recent years, the high losses and the low gain-plasmon coupling of the nanocavities remain big obstacles to their practical applications. To tackle these problems, it's better to recall the requirement of lasing - the gain material overlaps spatially and spectrally with the optical modes and the gain is high enough to compensate the cavity loss. The

#366082 https://doi.org/10.1364/OE.27.020597
Journal © 2019 Received 29 Apr 2019; revised 13 Jun 2019; accepted 19 Jun 2019; published 10 Jul 2019

Optics EXPRESS

process can be described by the cavity laser rate equation [11]:

$$\frac{ds}{dt} = \beta An + \beta\Gamma As(n - n_0) - \gamma s. \tag{1}$$

where $s$ is the photon number of a single laser mode, $A$ is the total spontaneous emission rate, $\beta$ is the probability of spontaneous emission transferred to the laser mode, $\Gamma$ is the overlap factor between optical modes and the gain region, $n$ is the carrier population in the excited state, $n_0$ is the carrier population at transparency, and $\gamma$ is the photon loss rate of the cavity. The first term on the right side of Eq. (1) accounts for spontaneously emitted photons coupled into the lasing mode, the second term for photons from stimulated emission and the last term for photon loss from the cavity. Obviously, the lasing process can be boosted by increasing $\beta$, $\Gamma$ and reducing $\gamma$.

Two routes are usually applied: One is improving the composition and/or configuration of metallic components to reduce the cavity loss $\gamma$ and increase gain-plasmon coupling ($\beta$, $\Gamma$), the other is using high gain materials to better compensate the cavity loss. For instance, silver is the best choice among all metals, because it has the lowest intrinsic loss in the full visible region [17]. Following the second route, the lasing threshold of a MIS nanolaser could be reduced from MW cm$^{-2}$ to W cm$^{-2}$ by replacing the CdS nanowire (optical gain 200 cm$^{-1}$) with InGaN/GaN core–shell nanorods (optical gain 10000 cm$^{-1}$) [12,18–19]. To control the LSP nanolaser, the additional key is the geometry of plasmonic nanostructures including the shape and dimensions of elements within a cavity, as well as the periodicity of the cavity array. It has been reported that, a pair of nanoparticles can be grouped together in a dielectric pit to form a bowtie gap, where the strongly localized electromagnetic (EM) field in the gap allows the occurrence of lasing at room temperature near the LSP resonance wavelength [20]. In a periodic array of plasmonic nanoparticles, the radiative losses can be suppressed effectively due to the coupling between LSP and lattice plasmon modes, through which photons scattered from one nanoparticle would be collected by adjacent nanoparticles as plasmons instead of decay into free-space [21]. Additionally, plasmon lasing with high tunability in wavelength [22] and mode number [23] has been achieved by engineering the dielectric constants of the liquid gain as well as the period and symmetry of the lattice array.

In this work, we propose that the radiative losses of the cavity can be significantly suppressed through increasing the density of plasmonic hot spots to accumulate the otherwise lost photons scattered by the device. This is achieved by the delicate design of 3D plasmonic metamaterials, i.e. placing the N-shaped silver wire and hole, respectively, on the bottom and top layers. Taking the advantage of sharp tips, edges and corners of the metallic structures, strongly coupled multiple hot spots, each with ultrahigh local density of EM states [24,25], can be generated at different locations. Moreover, as the wire-hole unit is arranged in a periodic array, the dielectric and metal are distributed in an alternate manner along both transverse and vertical directions, thereby leading to 3D confinement of local fields within subwavelength volumes; at the same time, the perfect spatial overlap of hot spots and gain media guarantees sufficient gain-plasmon coupling. Benefiting from these advantages, we experimentally demonstrate that lasing at low pump thresholds is realized [26], which can be even achieved in organic materials with very low optical gain. Importantly, the threshold as well as the emission intensity is subject to the density of hot spots which can be further tailored through varying the lattice constant of the metamaterial array. At last, the polarization of the laser emission is found to depend primarily on the oscillation direction of the dipolar modes hence can be controlled by the shape of the plasmonic nanostructures.

## 2. Design and simulation of metamaterial nanocavities

Our devices consist of metallic nanostructures on $SiO_2$/Si substrates as shown in Fig. 1. Two kinds of nanostructures are designed for comparison. One is silver nanorods arranged in a 2D

Optics EXPRESS

array and covered by a layer of ionic liquid (IL) that serves as the gain material (pink color in Figs. 1(a)–1(c)), which is referred as Device 1 ($D_1$). The periods of the 2D array are 200 and 350 nm in $x$ and $y$ directions respectively with nanorods tilted by an angle of 45° relative to the $x$ axis as shown in Fig. 1(b). The other is a 3D wire-hole array (Fig. 1(d)) consisting of N-shaped silver wires on the bottom and N-shaped nanoapertures on top with polymethylmethacrylate (PMMA) sandwiched in between (light blue in Figs. 1(d)–1(f)). The apertures are then filled by ionic liquid that together with PMMA works as gain media. The unique configuration of N-shaped wire-hole array allows the metal and dielectric to be placed in an alternate manner along both transverse ($x$) and vertical directions ($z$), which is favorable to suppress the scattering loss and at the same time maximize the overlap between the dielectric and plasmonic hot spots (Fig. 1(f)). In order to tailor the lasing behaviors, two sets of wire-hole arrays named as Devices 2 and 3 ($D_2$, $D_3$) were designed with large and small lattice constants denoted in Fig. 1(e), respectively. We then calculated spectral responses for the three devices using commercial finite-integration time-domain algorithm software (Lumerical solutions). The refractive indexes of silver, silicon and ionic liquid used in the calculation were obtained from the previous work [27–29].

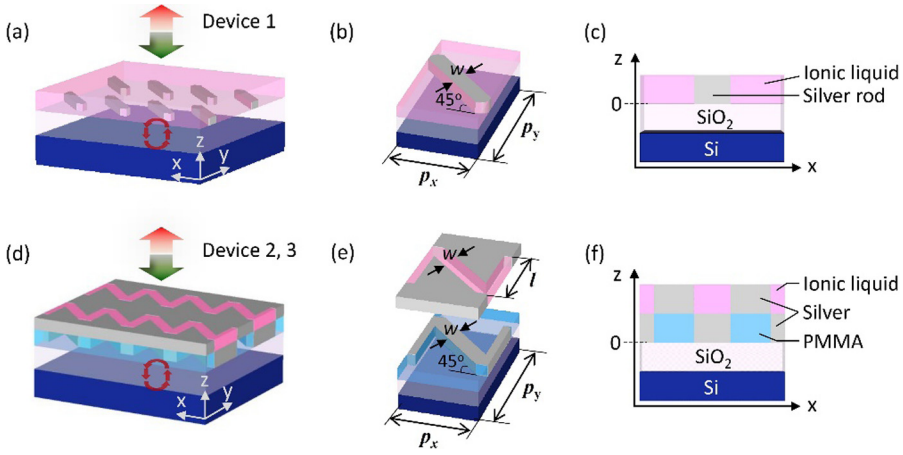


**Fig. 1.** (a) Device 1: a silver nanorod array on the $SiO_2$/Si substrate covered by a layer of ionic liquid. Green/red arrows denote the pump/emission, respectively. Circular red arrows represent the $SiO_2$/Si waveguide mode. (b) Unit cell for Device 1 with $p_x = 200$ nm, $p_y = 350$ nm, and $w = 40$ nm. (c) Cross-section of a unit cell for Device 1 with the cutting plane at the middle of the nanorod. (d) Devices 2 and 3: a 3D silver wire-hole array on the $SiO_2$/Si substrate with PMMA (light blue) and ionic liquid (pink) filled in. (e) Unit cell for Devices 2 and 3 which contains N shaped silver wire and hole on the bottom and top layer, respectively. Device 2: $p_x = 200$ nm, $p_y = 350$ nm, $l = 200$ nm, $w = 40$ nm and Device 3: $p_x = 150$ nm, $p_y = 250$ nm, $l = 150$ nm, and $w = 30$ nm. The thickness of silver, ionic liquid, PMMA and $SiO_2$ are 45, 45, 45 and 270 nm, respectively. (f) Cross-section of a unit cell for Devices 2 and 3 with the cutting plane at the middle of the wire-hole.

The simulated reflectance/absorption spectra of the three devices are shown in Figs. 2(a)–2(c) with the incident polarization fixed in the $x$ direction. For Device 1, the reflectance of the 2D rod array surrounded by ionic liquid (blue curve in Fig. 2(a)) shows two shallow dips at ~ 530 and 605 nm, indicating surface plasmon resonances are excited at both wavelengths. The distribution of normalized electric field at 605 nm within different cutting planes is shown in Fig. 2(d), where the fields are quite uniform (green background) except those localized around the edges of the metallic rods (yellow and red). In Device 2 with a 3D array, a pronounced resonance dip is observed at ~ 605 nm (blue curve in Fig. 2(b)) whose field distributions at

Optics EXPRESS

another set of cutting planes are shown in Fig. 2(e). It is found that local hot spots inside the dielectrics are periodically displaced in each layer and alternately distributed in the top and bottom layers (Fig. 2(f)), consistent with the principle of the lowest energy distribution of a system. Specifically, the electric fields are confined in the triangular tips of the bottom-layer dielectric and N shaped aperture of the top-layer dielectric, as depicted by the bottom and top slices in Fig. 2(e) respectively. At the interface of the two layers, the electric fields are strongly localized at the edges of metal wires as shown in the middle slice in Fig. 2(e). Although distributed at different locations, these hot spots are strongly coupled by in-phase oscillations.

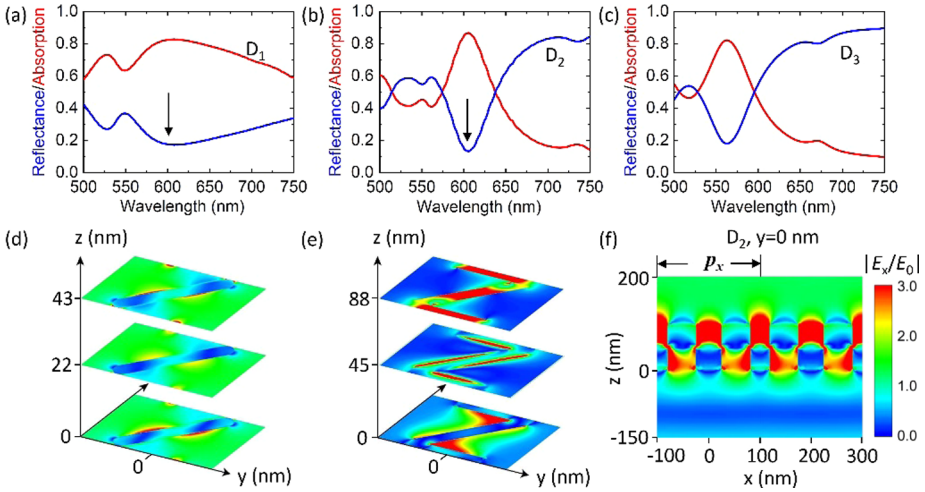


**Fig. 2.** (a-c) Simulated reflectance and absorption spectra of Device 1 (a), Device 2 (b), and Device 3 (c), respectively. (d) E-field distributions of a unit cell of Device 1 at $z = 1$, 22, and 43 nm cutting planes, $\lambda = 605$ nm. (e) E-field distributions of Device 2 at $z = 1$, 45 and 88 nm cutting planes, $\lambda = 605$ nm. (f) E-field distribution of Device 2 at the $y = 0$ nm cuting plane, $\lambda = 605$ nm.

To compare the effect of the field localization between 2D and 3D nanostructures, both $|E_{x\_max}|/|E_0|$ and $|E_{x\_max}|/|E_{x\_min}|$ are calculated, where the former is used to characterize the field enhancement relative to the incident field and the latter describes how hot a spot is compared with its environment. In Figs. 2(d) and 2(e), for the three slices from bottom to top, the field enhancement $|E_{x\_max}|/|E_0|$ is larger in magnitude for 3D (21, 13 and 17) than 2D (12, 3 and 12), representing higher local density of optical states in the hot spots of 3D nanostructures. As for $|E_{x\_max}|/|E_{x\_min}|$, the ratios are around 490, 190 and 300 for the 2D array, and increase strikingly to 19000, 6400, and 860 for the 3D array, suggesting the much weaker background, i.e. the greatly reduced scattering loss in the 3D nanostructure. In other words, the multiple hot spots enable the 3D wire-hole array to efficiently accumulate photons. As for Device 3, the distribution of electric field is similar to that of Device 2 except an obvious blue shift of the reflectance dip to $\sim$ 560 nm (blue curve in Fig. 2(c)) and a concomitant increase of density of hot spots due to the smaller structural lattice.

It is well known that the enhancement of the spontaneous emission rate of a quantum emitter by its environment can be characterized by the Purcell factor [30]. Here, the 3D metamaterials create an effective nanocavity with mode volume $V$, quality factor $Q$ and the Purcell factor enhancement of photoluminescence (PL):

$$F_p = \frac{3}{4\pi^2}\left(\frac{\lambda}{n}\right)^3 \frac{Q}{V}. \tag{2}$$

Optics EXPRESS

where $n$ is the medium's refractive index that is ~ 1.43 for both ionic liquid and PMMA in the present case. The $Q$ factor is characterized as a resonator's bandwidth relative to its central wavelength, here defined as $Q = \lambda/\Delta\lambda$ in which $\Delta\lambda$ is the full width at half maximum (FWHM) of the absorption peak as shown by the red curves in Figs. 2(b) and 2(c). The mode volume $V$, *i.e.* the volume of strongly localized fields, is obtained from the volume of the hot spots in a unit cell. For the central wavelength 605 and 560 nm, where the absorption peaks appear, the Purcell factors are calculated to be ~ 60 and 85 for Devices 2 and 3, respectively. Hence, Device 3 with a higher Purcell factor than Device 2 due to the smaller mode volume, is expected to have a stronger influence on the spontaneous emission rate of the gain material.

## 3. Experiment

### 3.1. Device fabrication and spectral measurement

To investigate the plasmonic resonance and its correlation with the PL emission, we implemented the above three proposals using state-of-art electron beam lithography and metal deposition. Note that the liftoff process is only applied to Device 1 to remove the PMMA, whereas PMMA is kept in Devices 2 and 3. In addition, a thinner PMMA resist is used for Devices 2 and 3 to guarantee the narrow aperture width as well as the connection between top and bottom metallic structures. The scanning electron microscopy (SEM) images of the metamaterial structures for Devices 1-3 are shown in Fig. 3(a). The measured reflectance spectra are shown in Fig. 3(d) which agree qualitatively with the simulations in Figs. 2(a)–2(c). For PL measurement, the devices are optically pumped by a continuous-wave solid state laser (532 nm) polarized along the $x$ direction which is focused by a 50 × objective lens to a ~ 5 × 5 μm$^2$ spot with 500 μW pump power. Then PL spectra are collected and dispersed with a spectrometer (Andor SR500) and finally detected by a CCD (iDus 420) camera.

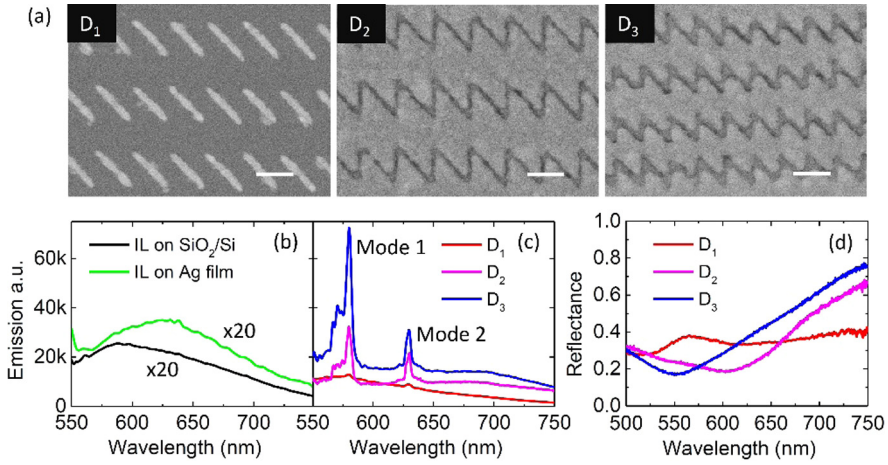


**Fig. 3.** (a) SEM images of Devices 1-3, white scale bar is 200 nm. (b) Measured emission spectra of bare ionic liquid (IL) on $SiO_2$/Si (black curve) and 45 nm thick Ag film (green curve). (c) Measured emission spectra of Devices 1-3. (d) Measured reflectance spectra of Devices 1-3 illuminated by the white light.

The PL spectrum of a thin layer of ionic liquid N,N-Diethyl-N-methyl-N-(2-methoxyethyl)ammonium bis(trifluoromethanesulfonyl)imide (DEME-TFSI) on the $SiO_2$/Si substrate was firstly measured as a reference (black curve in Fig. 3(b)). The ionic liquid consists of organic components which are able to emit photons over a broad bandwidth from 535 to 750 nm with the PL peak at 630 nm, consistent with the PL spectrum of ionic liquid on Ag film as shown by the green curve in

Optics EXPRESS

Fig. 3(b). The emission peak around 580 nm in the black curve arises from the waveguide mode of ionic liquid-$SiO_2$-Si multilayers, which is broad and of low intensity due to the very small difference in refractive index between the ionic liquid and $SiO_2$.

When the metamaterial arrays are embedded into the ionic liquid, the plasmonic resonance of the nanostructure couples with the waveguide modes of $SiO_2$/Si to support the cavity feedback of the system. For Device 1, the emission intensity (red curve in Fig. 3(c)) is found to be ~ 10 times stronger than that of the bare ionic liquid (black curve in Fig. 3(b)). This is due to surface plasmon resonances of the 2D rod array, manifested by two reflectance dips (red curve in Fig. 3(d)) that locate around the excitation and emission fields, respectively. As a result, the optical absorption and spontaneous emission of the gain material are simultaneously enhanced. Closer examination of the emission spectrum of Device 1 indicates that two cavity modes 1 and 2 are visible at 580 and 630 nm, as shown by the red curve in Fig. 3(c). These two modes originate from the hybrid plasmonic modes generated by the coupling between the plasmonic mode of the metamaterial and the waveguide modes of the $SiO_2$/Si substrate, whose spectral positions could be determined by the waveguide resonances. Roughly, the device is assumed to be a standard metal-dielectric-metal FP resonator. Define the frequency separation between the two modes $\Delta\nu$ as $c/2nL$ where $c$ is the speed of light, $L$ the thickness of $SiO_2$ and $n$ the group index of the system. For $\Delta\nu$ = 41 THz observed experimentally, the corresponding group index $n$ for our plasmonic nanocavity is about 13, similar to the case of a nanowire on the metallic film [12]. However, the two modes seem difficult to be narrowed and amplified, which could be explained by the inefficient gain-plasmon coupling and the weak field localization in the 2D array (Fig. 2(d)).

When the 2D rod array is replaced by the 3D wire-hole array, they become sharper as shown by the pink and blue curves in Fig. 3(c). For Device 2, the intensities are 25 and 17 times enhanced (pink curve in Fig. 3(c)) compared to those of the bare ionic liquid at 580 and 630 nm. The abrupt increase of the emission peak is probably due to the following reasons. First, the local field enhancement at the emitters arises from the extremely strong field confinement in the narrow slits as well as sharp tips of the N shaped PMMA holes (Fig. 2(e)). Second, the gain-plasmon coupling is quite efficient due to the distribution of hot spots inside the gain regions of the cavity. Third, the coupling between plasmons and waveguide modes of the substrate effectively inhibits the scattering loss and enhances the feedback of the cavity. Hence, the energy harvested by the 3D metamaterial can be transferred to the hybrid plasmonic modes and amplified to compensate for the loss of the system, resulting in the dramatic increase of emission peaks.

Different from Device 2, Device 3 has a smaller lattice constant of ($p_x$ = 150 nm, $p_y$ = 250 nm) whose SEM image is shown in Fig. 3(a). It exhibits the maximal emission intensity among the three devices, which is ~ 56 and 24 folds (blue curve in Fig. 3(c)) enhanced relative to those of the bare ionic liquid at 580 and 630 nm respectively. This is attributed to the increase of the density of hot spots, where it is ~ 1.9 times higher in Device 3 than Device 2 caused by the lattice shrinking. In addition, the LSP mode is blue shifted to 550 nm for Device 3 which is closer to the pump field (532 nm), thus the absorption of the gain is expected to be enhanced accordingly. Indeed, the emission intensity of mode 1 of Device 3 is found to be ~ 2.2 times stronger than that of Device 2. In short, the density of hot spots hence the emission intensity, can be further optimized by varying the structural lattice of the metamaterial structure.

### 3.2. Emission spectra as a function of pump power

To have a comprehensive understanding of emission behaviors of the three devices, emission spectra were measured as a function of pump power. Take the ionic liquid on the $SiO_2$/Si substrate as a reference, the emission spectra are depicted in Fig. 4a. The peak value extracted at 580 nm as a function of pump power is shown in Fig. 4b which exhibits a fast increase below 0.4 kW $cm^{-2}$, then slows down and becomes almost saturated at ~ 2 kW $cm^{-2}$. This behavior resembles the amplified spontaneous emission (ASE) assisted by a waveguide mode from the substrate

Optics EXPRESS

[31]. The saturation of the emission intensity is probably due to the intrinsic absorption limit of molecules and the amount of the gain material.

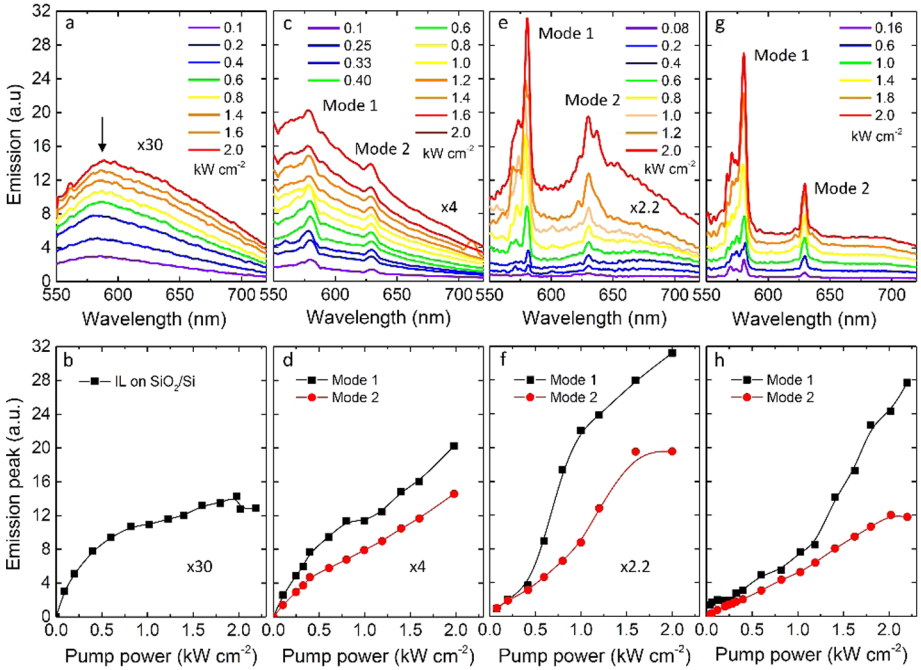


**Fig. 4.** First row: Emission spectra at different pump powers. Second row: Peak values of mode 1 at 580 nm (black squares) and mode 2 at 630 nm (red dots), as a function of pump power. From left to right, ionic liquid on $SiO_2$/Si (a, b), Device 1 (c, d), Device 2 (e, f) and Device 3 (g, h).

In Device 1, two cavity modes at 580 and 630 nm are visible (Fig. 4c) due to the coupling of plasmonic nanorods with the substrate waveguide. The peak values as a function of pump power are shown in Fig. 4d. Mode 1 experiences a fast linear increase below 0.4 kW $cm^{-2}$, and then slows down (black squares in Fig. 4d), suggesting that the emission is dominated by spontaneous rather than stimulated emission. Similar behaviors are observed for mode 2 (red dots in Fig. 4d). It is notable that the emission intensity keeps increasing without saturation above 0.4 kW $cm^{-2}$, indicating that the spontaneous emission rate can be boosted by the 2D rod array due to the Purcell effect, leading to the ASE with a higher upper limit of the saturation power. Nevertheless, the lasing is still not achieved, until the 2D nanorod array is replaced by the 3D wire-hole array in Devices 2 and 3.

In Device 2, the dependence of the emission peak on pump power shows a clear threshold behavior at 0.4 kW $cm^{-2}$ for mode 1, suggesting the occurrence of lasing (Fig. 4f). The achievement can be attributed to the ultrastrong feedback of the LSP-assisted cavity mode 1 and the efficient energy transfer from excited gains to this hybrid plasmonic mode. For mode 2, the threshold behavior is not as obvious as that of mode 1, suggesting that the coupling between LSP and the waveguide mode is less strong. In Device 3, a clear threshold is also observed for mode 1 but not for mode 2 (Fig. 4 h), because mode 2 at 630 nm is far away from the LSP mode at ~ 550 nm thus is less influenced. The threshold power 1.2 kW $cm^{-2}$ is higher than that of Device 2, which may be caused by the reduction of the total gain volume and the larger intrinsic loss of the surface plasmon resonance at higher frequencies.

Optics EXPRESS

In summary, spectral changes from amplified spontaneous emission to lasing can be realized by tailoring the metamaterial structures from 2D to 3D. The lasing characteristics, including threshold, intensity increase and narrowing of the emission peak, are able to be further optimized by adjusting the lattice constant of the 3D metamaterial structure.

### 3.3. Polarization of the emission for Devices 1 and 2

To resolve the polarization of the emission spectra, the polarizer is rotated to be parallel or perpendicular to the *x* direction, respectively. Since the energy transfer between the gain and plasmon involves resonantly coupled transitions [16], the polarization of the surface plasmon is expected to be preserved in the excitonic emission.

In Device 1, The PL spectra in *x* and *y* polarization directions coincide well with each other as shown in Fig. 5(a) resulting in a linearity $(I_x\text{-}I_y)/(I_x+I_y)$ close to zero as shown in Fig. 5(c). In contrast, the laser emission of Device 2 exhibits a big difference between *x* and *y* components as shown in Fig. 5(b) leading to a maximum linearity ~ 70% at 580 nm (black arrow in Fig. 5(d)). Correspondingly, the reflectance spectra of *x* and *y* polarizations for Device 1 are almost equivalent (Fig. 5(e)), whereas in Device 2, the reflectance difference for the wire-hole array between *x* and *y* polarizations is dramatic.

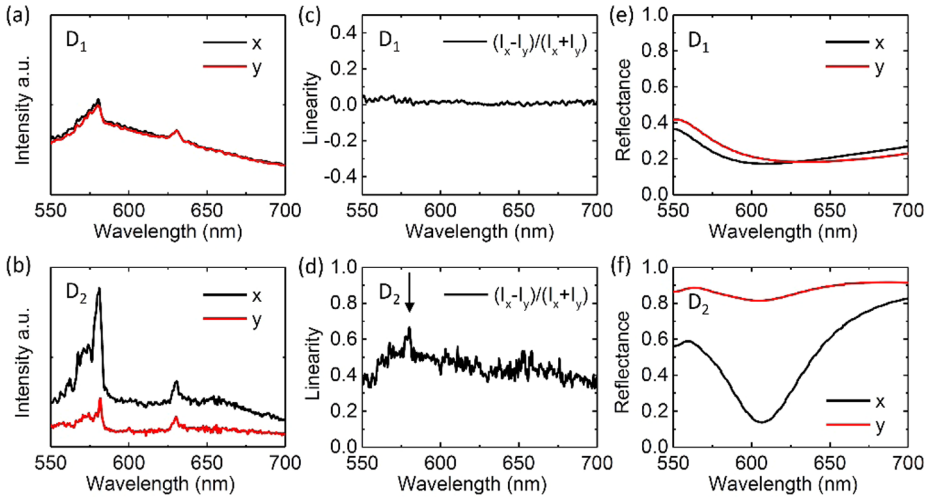


**Fig. 5.** (a, b) Emission spectra of Devices 1 and 2 collected along *x* and *y* directions respectively with the pump power fixed at 0.8 kW $cm^{-1}$. (c, d) Linearity of the emission of Devices 1 and 2. (e, f) Simulated reflectance spectra of Devices 1 and 2 with incident light polarized along *x* and *y* polarizations.

The spectral distinction may find the origin from their structures. The nanorods in Device 1 are tilted by 45°, so that orthogonally polarized electric dipolar resonances are excited leading to the equal amount of emission in *x* and *y* directions, consistent with the result shown in Fig. 5(a). The N shaped wire-hole array exhibits a strong LSP resonance in the *x* polarization direction, hence the laser emission induced by the LSP is polarized along the same direction (Fig. 5(b)). As a result, the emission is random for Device 1 and linearly polarized for Device 2. The strong correlation between the geometry of plasmonic nanostructures and the spectral performance is instructive for implementing nanolasers of different polarizations.

Optics EXPRESS

## 4. Discussion

The most striking feature of the above 3D metamaterial nanolaser is the very low requirement of the material gain, as evidenced by the ionic liquid used above that has emission intensity ~ 500 times weaker than a typical dye (*e.g.* Rhodamine 6G whose optical gain is ~ 3000 $cm^{-1}$ [32]). This benefits from three advantages of the N-shaped wire-hole nanocavity. First, the scattering losses are strongly suppressed by densely distributing the metal and dielectric in an alternate manner along both transverse ($x$) and vertical ($z$) directions because the scattered photons can be captured at once by the strongly coupled plasmons nearby [33]. Second, multiple hot spots overlap perfectly with the gain media enabling efficient gain-plasmon coupling and hence sufficient energy transfer from the spontaneous to lasing mode. Third, strong confinement of the electric field in a volume well below the diffraction limit due to the sharp tips and narrow slits of the N-shaped wire-hole nanostructure leads to a high Purcell factor to increase the stimulated emission cross section of the gain material [20]. Hence, lasing can be realized in a material with an ultralow efficiency of excitonic emission.

We noted that besides the ionic liquid, the PMMA in 3D wire-hole array also plays a role as the gain medium. It has been reported that the irradiation by high-energy electrons or laser beams on PMMA results in fluorescent moieties [34] whose emission spectrum spans from 550 to 750 nm [35]. That's why two emission peaks remain observable (but not lasing) at 580 and 630 nm when removing the ionic liquid. This is also consistent with the scenario of highly localized fields in the hot spots of our system, where the strong fields cause the generation of fluorescent moieties.

In practical applications, lasing with strong directional preference is very important for the integrated photonic circuits. Directional emission normal to the plane of the array has been shown in SPASER consisting of 2D periodic nanohole array due to the formation of in-phase dipolar resonances of the nanoholes in parallel with the array plane [36–38]. Similarly, in our wire-hole array, the LSP is dominated by the electrical dipolar resonance in the $x$ direction, along which all the plasmonic units oscillate in phase. Hence the emission is expected to be fixed along the direction perpendicular to the array plane.

## 5. Conclusion

In conclusion, inducing lasing in organic materials with a low optical gain is achieved in 3D metamaterial array because of the high density of hot spots, ultrastrong field confinement as well as the sufficient overlap between surface plasmons and gain media. The emission behaviors of the plasmonic nanocavity depend very much on the density of hot spots which can be controlled by the dimensionality and lattice constant of the metamaterials. By tailoring the metamaterials from 2D to 3D, the amplified spontaneous emission is found to evolve into lasing. The emission intensity and lasing threshold are able to be further optimized by adjusting the lattice constant of 3D metamaterial arrays: the smaller lattice with a shorter plasmon wavelength exhibits a higher emission intensity but a higher lasing threshold. In addition, the polarization of the emission is consistent with the resonant direction of the plasmonic field which can be controlled by the geometry of the plasmonic nanostructure. Our study provides a proof-of-concept 3D plasmonic metamaterial nanolaser, with the characteristics of ultralow gain requirement, high tunability, and fixed beam direction, paving the way towards on-chip integrated plasmonic circuits for fast communication and bimolecular sensing.

## Funding

H2020 European Research Council (ERC) (648855 Ig-QPD); CAS Pioneer Hundred Talents Program, China.

Optics EXPRESS

## References


1. M. T. Hill and M. C. Gather, "Advances in small lasers," Nat. Photonics **8**(12), 908–918 (2014).
2. R. M. Ma, S. Ota, Y. Li, S. Yang, and X. Zhang, "Explosives detection in a lasing plasmon nanocavity," Nat. Nanotechnol. **9**(8), 600–604 (2014).
3. T. Kim, J. G. McCall, Y. H. Jung, X. Huang, E. R. Siuda, Y. Li, J. Song, Y. M. Song, H. A. Pao, R.-H. Kim, C. Lu, S. D. Lee, I.-S. Song, G. Shin, R. Al-Hasani, S. Kim, M. P. Tan, Y. Huang, F. G. Omenetto, J. A. Rogers, and M. R. Bruchas, "Injectable, cellular-scale optoelectronics with applications for wireless optogenetics," Science **340**(6129), 211–216 (2013).
4. R.-M. Ma and R. F. Oulton, "Applications of nanolasers," Nat. Nanotechnol. **14**(1), 12–22 (2019).
5. D. Saxena, S. Mokkapati, P. Parkinson, N. Jiang, Q. Gao, H. H. Tan, and C. Jagadish, "Optically pumped room-temperature GaAs nanowire lasers," Nat. Photonics **7**(12), 963–968 (2013).
6. Y. Ye, Z. Wong, X. Lu, X. Ni, H. Zhu, X. Chen, Y. Wang, and X. Zhang, "Monolayer excitonic laser," Nat. Photonics **9**(11), 733–737 (2015).
7. K. Takeda, T. Sato, A. Shinya, and K. Nozaki, "Few-fJ/bit data transmissions using directly modulated lambda-scale embedded active region photonic-crystal lasers," Nat. Photonics **7**(7), 569–575 (2013).
8. M. T. Hill, Y. S. Oei, B. Smalbrugge, Y. Zhu, T. D. Vries, P. J. V. Veldhoven, F. W. M. V. Otten, T. J. Eijkemans, J. P. Turkiewicz, H. D. Waardt, E. J. Geluk, S. H. Kwon, Y. H. Lee, R. Nötzel, and M. K. Smit, "Lasing in metallic-coated nanocavities," Nat. Photonics **1**(10), 589–594 (2007).
9. M. A. Noginov, G. Zhu, A. M. Belgrave, R. Bakker, V. M. Shalaev, E. E. Narimanov, S. Stout, E. Herz, T. Suteewong, and U. Wiesner, "Demonstration of a spaser-based nanolaser," Nature **460**(7259), 1110–1112 (2009).
10. D. J. Bergman and M. I. Stockman, "Surface plasmon amplification by stimulated emission of radiation: quantum generation of coherent surface plasmons in nanosystems," Phys. Rev. Lett. **90**(2), 027402 (2003).
11. R.-M. Ma, R. F. Oulton, V. J. Sorger, and X. Zhang, "Plasmon lasers: Coherent light source at molecular scales," Laser Photonics Rev. **7**(1), 1–21 (2013).
12. R. F. Oulton, V. J. Sorger, T. Zentgraf, R. M. Ma, C. Gladden, L. Dai, G. Bartal, and X. Zhang, "Plasmon lasers at deep subwavelength scale," Nature **461**(7264), 629–632 (2009).
13. R. M. Ma, R. F. Oulton, V. J. Sorger, G. Bartal, and X. Zhang, "Room-temperature sub-diffraction-limited plasmon laser by total internal reflection," Nat. Mater. **10**(2), 110–113 (2011).
14. S. Wang, X. Y. Wang, B. Li, H. Chen, Y. L. Wang, L. Dai, R. F. Oulton, and R. M. Ma, "Unusual scaling laws for plasmonic nanolasers beyond the diffraction limit," Nat. Commun. **8**(1), 1889 (2017).
15. X. Meng, A. V. Kildishev, K. Fujita, K. Tanaka, and V. M. Shalaev, "Wavelength-tunable spasing in the visible," Nano Lett. **13**(9), 4106–4112 (2013).
16. W. Zhou, M. Dridi, J. Y. Suh, C. H. Kim, D. T. Co, M. R. Wasielewski, G. C. Schatz, and T. W. Odom, "Lasing action in strongly coupled plasmonic nanocavity arrays," Nat. Nanotechnol. **8**(7), 506–511 (2013).
17. D. Li and M. I. Stockman, "Electric spaser in the extreme quantum limit," Phys. Rev. Lett. **110**(10), 106803 (2013).
18. Y. J. Lu, C. Y. Wang, J. Kim, H. Y. Chen, M. Y. Lu, Y. C. Chen, W. H. Chang, L. J. Chen, M. I. Stockman, C. K. Shih, and S. Gwo, "All-color plasmonic nanolasers with ultralow thresholds: autotuning mechanism for single-mode lasing," Nano Lett. **14**(8), 4381–4388 (2014).
19. S. Gwo and C.-K. Shih, "Semiconductor plasmonic nanolasers: current status and perspectives," Rep. Prog. Phys. **79**(8), 086501 (2016).
20. J. Y. Suh, C. H. Kim, W. Zhou, M. D. Huntington, D. T. Co, M. R. Wasielewski, and T. W. Odom, "Plasmonic bowtie nanolaser arrays," Nano Lett. **12**(11), 5769–5774 (2012).
21. D. Wang, W. Wang, M. P. Knudson, G. C. Schatz, and T. W. Odom, "Structural engineering in plasmon nanolasers," Chem. Rev. **118**(6), 2865–2881 (2018).
22. A. Yang, T. B. Hoang, M. Dridi, C. Deeb, M. H. Mikkelsen, G. C. Schatz, and T. W. Odom, "Real-time tunable lasing from plasmonic nanocavity arrays," Nat. Commun. **6**(1), 6939 (2015).
23. D. Wang, A. Yang, W. Wang, Y. Hua, R. D. Schaller, G. C. Schatz, and T. W. Odom, "Band-edge engineering for controlled multi-modal nanolasing in plasmonic superlattices," Nat. Nanotechnol. **12**(9), 889–894 (2017).
24. V. Giannini, A. I. Fernández-Domínguez, S. C. Heck, and S. A. Maier, "Plasmonic nanoantennas: fundamentals and their use in controlling the radiative properties of nanoemitters," Chem. Rev. **111**(6), 3888–3912 (2011).
25. L. Novotny and B. Hecht, *Principles of Nano-Optics* (Cambridge University, 2006).
26. S. Wu, S. Buckley, J. R. Schaibley, L. Feng, J. Yan, D. G. Mandrus, F. Hatami, W. Yao, J. Vučković, A. Majumdar, and X. Xu, "Monolayer semiconductor nanocavity lasers with ultralow thresholds," Nature **520**(7545), 69–72 (2015).
27. C. Han, L. Yang, P. Ye, E. P. J. Parrott, E. Pickwell-Macpherson, and W. Y. Tam, "Three dimensional chiral plasmon rulers based on Ag nanorod trimers," Opt. Express **26**(8), 10315–10325 (2018).
28. M. A. Green, "Self-consistent optical parameters of intrinsic silicon at 300 K including temperature oefficients," Sol. Energy Mater. Sol. Cells **92**(11), 1305–1310 (2008).
29. S. Seki, S. Tsuzuki, K. Hayamizu, Y. Umebayashi, N. Serizawa, K. Takei, and H. Miyashiro, "Comprehensive refractive index property for room-temperature ionic liquids," J. Chem. Eng. Data **57**(8), 2211–2216 (2012).
30. K. Tanaka, E. Plum, J. Y. Ou, T. Uchino, and N. I. Zheludev, "Multifold enhancement of quantum dot luminescence in plasmonic metamaterials," Phys. Rev. Lett. **105**(22), 227403 (2010).
31. D. Pisignano, E. Mele, L. Persano, G. Paladini, and R. Cingolani, "Amplified spontaneous emission from a conjugated polymer undergone a high-temperature lithography cycle," Appl. Phys. Lett. **86**(26), 261104 (2005).

Optics EXPRESS


32. M. A. Noginov, V. A. Podolskiy, G. Zhu, M. Mayy, M. Bahoura, J. A. Adegoke, B. A. Ritzo, and K. Reynolds, "Compensation of loss in propagating surface plasmon polariton by gain in adjacent dielectric medium," Opt. Express **16**(2), 1385–1392 (2008).
33. C. Han and W. Y. Tam, "Broadband optical magnetism in chiral metallic nanohole arrays by shadowing vapor deposition," Appl. Phys. Lett. **109**(25), 251102 (2016).
34. D. L. N. Kallepalli, A. M. Alshehri, D. T. Marquez, L. Andrzejewski, J. C. Scaiano, and R. Bhardwaj, "Ultra-high density optical data storage in common transparent plastics," Sci. Rep. **6**(1), 26163 (2016).
35. B. F. Howell and M. G. Kuzyk, "Amplified spontaneous emission and recoverable photodegradation in polymer doped with Disperse Orange 11," J. Opt. Soc. Am. B **19**(8), 1790–1973 (2002).
36. X. Meng, J. Liu, A. V. Kildishev, and V. M. Shalaev, "Highly directional spaser array for the red wavelength region," Laser Photonics Rev. **8**(6), 896–903 (2014).
37. A. V. Dorofeenko, A. A. Zyablovsky, A. P. Vinogradov, E. S. Andrianov, A. A. Pukhov, and A. A. Lisyansky, "Steady state superradiance of a 2D-spaser array," Opt. Express **21**(12), 14539–14547 (2013).
38. A. Yang, Z. Li, M. P. Knudson, A. J. Hryn, W. Wang, K. Aydin, and T. W. Odom, "Unidirectional lasing from template-stripped two-dimensional plasmonic crystals," ACS Nano **9**(12), 11582–11588 (2015).